Super-Energy-Resolution Material Decomposition for Spectral Photon-Counting CT Using Pixel-Wise Learning

Bingqing Xie, Yuemin Zhu, Pei Niu, Ting Su, Feng Yang, Lihui Wang, Pierre-Antoine Rodesch, Loic Boussel, Philippe Douek, Philippe Duvauchelle

▶ **To cite this version:**

Bingqing Xie, Yuemin Zhu, Pei Niu, Ting Su, Feng Yang, et al.. Super-Energy-Resolution Material Decomposition for Spectral Photon-Counting CT Using Pixel-Wise Learning. IEEE Access, 2021, 9 (3), pp.168485 - 168495. 10.1109/access.2021.3134636 . hal-04455271

HAL Id: hal-04455271
https://hal.science/hal-04455271v1

Submitted on 13 Feb 2024

HAL is a multi-disciplinary open access archive for the deposit and dissemination of scientific research documents, whether they are published or not. The documents may come from teaching and research institutions in France or abroad, or from public or private research centers.

L'archive ouverte pluridisciplinaire **HAL**, est destinée au dépôt et à la diffusion de documents scientifiques de niveau recherche, publiés ou non, émanant des établissements d'enseignement et de recherche français ou étrangers, des laboratoires publics ou privés.

IEEE Access
Multidisciplinary ⋮ Rapid Review ⋮ Open Access Journal

Received November 9, 2021, accepted December 1, 2021, date of publication December 10, 2021,
date of current version December 29, 2021.

Digital Object Identifier 10.1109/ACCESS.2021.3134636

Super-Energy-Resolution Material Decomposition for Spectral Photon-Counting CT Using Pixel-Wise Learning

BINGQING XIE[1], YUEMIN ZHU[1], PEI NIU[1], TING SU[2], FENG YANG[3], LIHUI WANG[4], PIERRE-ANTOINE RODESCH[5], LOIC BOUSSEL[5], PHILIPPE DOUEK[5], AND PHILIPPE DUVAUCHELLE[6]

[1]Centre National de la Recherche Scientifique (CNRS), CREATIS UMR 5220, U1294, INSA Lyon, Inserm, University of Lyon, 69621 Lyon, France
[2]Research Center for Medical Artificial Intelligence, Shenzhen Institutes of Advanced Technology, Chinese Academy of Sciences, Shenzhen 518055, China
[3]Lister Hill National Center for Biomedical Communications, National Library of Medicine (NLM), National Institutes of Health (NIH), Bethesda, MD 20892, USA
[4]Key Laboratory of Intelligent Medical Image Analysis and Precise Diagnosis of Guizhou Province, School of Computer Science and Technology, Guizhou University, Guiyang 550025, China
[5]CREATIS, CNRS, Radiology Department, Hospices Civils de Lyon, Inserm, INSA-Lyon, University of Lyon, 69007 Lyon, France
[6]Laboratoire Vibrations Acoustique (LVA), INSA Lyon, University of Lyon, 69621 Villeurbanne, France

Corresponding author: Yuemin Zhu (yuemin.zhu@creatis.insa-lyon.fr)

This work was supported in part by the Program Hubert Curien Partnerships (PHC)-Cai Yuanpei 2018 under Grant 41400TC, in part by the International Research Project Modélisation et traitement d'images et du signal pour la Santé (METISLAB), in part by the Committee of Science and Technology of Shanghai under Grant 19510711200, in part by the European Union Horizon 2020 under Grant 643694, and in part by the Project Point Accueil Installation (PAI) Region Auvergne-Rhone-Alpes under Grant 2000688501-40890.

ABSTRACT Spectral photon-counting CT offers novel potentialities to achieve quantitative decomposition of material components, in comparison with traditional energy-integrating CT or dual-energy CT. Nonetheless, achieving accurate material decomposition, especially for low-concentration materials, is still extremely challenging for current sCT, due to restricted energy resolution stemming from the trade-off between the number of energy bins and undesired factors such as quantum noise. We propose to improve material decomposition by introducing the notion of super-energy-resolution in sCT. The super-energy-resolution material decomposition consists in learning the relationship between simulation and physical phantoms in image domain. To this end, a coupled dictionary learning method is utilized to learn such relationship in a pixel-wise way. The results on both physical phantoms and in vivo data showed that for the same decomposition method using lasso regularization, the proposed super-energy-resolution method achieves much higher decomposition accuracy and detection ability in contrast to traditional image-domain decomposition method using L1-norm regularization.

INDEX TERMS X-ray CT, material decomposition, photon-counting detector, super energy resolution.

I. INTRODUCTION

Spectral photon-counting X-ray computed tomography (sCT) provides additional X-ray spectrum information about material components in an organ or tissue, due to its ability of separating photons into different energy bins by using photon-counting detector (PCD). This ability makes possible efficient material decomposition of which the objective is to quantitatively measure different materials encoded by a pixel.

It is a huge challenge to obtain high accuracy of material decomposition in clinical applications, especially for low-concentration materials [1], [2]. This is linked to the principle itself of sCT. With respect to conventional CT or dual-energy CT (DECT) to some extent, sCT divides the assayed energy range into discrete energy bins. An increased number of energy bins correlates with an increased spectral resolution, although this might simultaneously contribute to a reduced signal-noise ratio (SNR), due to a smaller number of photons being collected in each energy bin. Many aspects can influence the accuracy of material decomposition, including exposure time, energy bin width, acceptable flux rate, *etc*. Although there is complex interdependency between the parameters, we will focus on energy bin that is a basic parameter for spectral CT in contrast to conventional CT. In other words, energy resolution of sCT is limited by a trade-off

The associate editor coordinating the review of this manuscript and approving it for publication was Kathiravan Srinivasan.

This work is licensed under a Creative Commons Attribution 4.0 License. For more information, see https://creativecommons.org/licenses/by/4.0/

between the total number of energy bins and the image quality in each bin, which restricts the accuracy of material decomposition and ability of detecting low-concentration materials.

Existing material decomposition methods can be divided into three categories: projection-domain [3]–[6], image-domain [6]–[11] and one-step material decomposition [12]–[14], according to the sequence of material decomposition and image reconstruction, *i.e.* before, after or during. Most decomposition methods of all the three ways try to improve performance of material decomposition by exploiting the high correlation between spectral and spatial features embedded in the multi-energy images. However, almost no work can be found in the literature to enhance energy resolution of sCT by software. Actually, for DECT, there is an imaging method that aims to enhance the visibility of contrast agent by reconstructing the image at one chosen computed energy, called virtual monochromatic image (mono-E or VMS) [15]. The performance of mono-E from DECT is determined by the material decomposition that is processed only on actual images, which is noisy and depends on the chosen computed energy.

In this paper, we propose to introduce the notion of super-energy-resolution (SER) into sCT in order to improve the accuracy of material decomposition in image domain. The idea is to learn the relationship between spectral features of simulated data and those of physical data, then applying it to other physical data. To do it, theoretical sCT images containing abundant spectral energy information, designated as SER images, are simulated according to physical phantoms. The mapping between actual sCT images and SER images are learned by utilizing a coupled dictionary learning (CDL) method in a pixel-wise way. SER images synthesized based on the learned mapping are then used for material decomposition in image domain.

II. MODEL AND METHOD

Common models of image-domain material decomposition are firstly shown in this section. Then, SER for sCT is introduced and modeled. At last, the proposed SER-based material decomposition is described.

A. MODELS OF IMAGE-DOMAIN MATERIAL DECOMPOSITION

Tomography reconstruction, which is a preliminary step for image-domain material decomposition methods, is separately processed at each individual bin. Reconstruction at the i-th energy bin tries to achieve the spatial image, *i.e.* the linear attenuation coefficients (LAC) $\mu(\vec{x}, i)$ at pixel $\vec{x}$:

$$\mu(\vec{x}, i) = \underset{\mu}{\operatorname{argmin}}\, \mathcal{D}(\mathcal{C}(s_i(u)), \mu(\vec{x}, i)) + R, \tag{1}$$

where $s_i(u)$ represents the recorded photons along the u-th ray in the i-th energy bin, $\mathcal{C}$ the mapping function between $s_i(u)$ and LAC, $\mathcal{D}$ the data-fidelity term, and R the regularization. The detailed relationship between $\boldsymbol{\mu}$ and $\boldsymbol{s}$, *i.e.* $\mathcal{C}$ in equation (1), is described by:

$$\bar{s}_i(u) = \int_{\mathbb{R}} n_0(E) d_i(E) e^{-\int_{L(u)} \mu(\vec{x}, E) \mathrm{d}l} \mathrm{d}E, \tag{2}$$

where $\bar{s}_i(u)$ denotes the mean value of $s_i(u)$, $n_0(E)$ the incident photon fluence from X-ray source, $L(u)$ the u-th ray, $\mu(\vec{x}, E)$ the LAC at energy E, and $d_i(E)$ the detector absorption efficiency or detector response function that can give the probability of a photon of energy E to be measured within bin i [3]. For X-ray CT images, noise level is negatively related to the square root of the total number of detected photons [16]. In other words, sCT suffers from stronger quantum noise for narrower bin.

Material decomposition is then performed on the reconstructed multi-energy images:

$$\mu(\vec{x}, i) = \sum_{\alpha=1}^{M} \dot{\mu}_{m\alpha}(i) \rho_\alpha(\vec{x}), \quad i = 1, \ldots, B, \tag{3}$$

where subscript α denotes the α-th basis material, $\dot{\mu}_{m\alpha}(i)$ the calculated i-th energy-bin effective mass attenuation coefficient (MAC), B the number of energy bins, M the number of basis materials, and $\rho_\alpha(\vec{x})$ the mass density at pixel $\vec{x}$. We rewrite image-domain material decomposition into its matrix form as:

$$\boldsymbol{Y} = \boldsymbol{M}\boldsymbol{X} + \boldsymbol{N}, \tag{4}$$

where $\boldsymbol{Y} \in \mathcal{R}^{B \times N_P}$ designates the reconstructed multi-energy spatial images of $\boldsymbol{\mu}$ with N_P designating the number of pixels or voxels, $\boldsymbol{M} \in \mathcal{R}^{B \times M}$ the decomposition matrix of $\boldsymbol{\mu_m}$, $\boldsymbol{X} \in \mathcal{R}^{M \times N_P}$ the decomposed basis material images of mass densities $\boldsymbol{\rho}$ and $\boldsymbol{N}$ the noise.

Consequently the aforementioned trade-off between the number of energy bins and noise level leads to limited energy resolution in sCT. In practice, the number of energy bins of sCT is generally scheduled by manufacturers, *e.g.* 5 bins for Phillips sCT prototype [17].

B. SUPER-ENERGY-RESOLUTION IMAGING IN sCT

We propose to improve the energy resolution by means of fully exploiting both simulation data and physical data. To do it, the notion of SER is introduced in sCT.

SER images are virtual multi-energy images with much more bins but noise-reduced compared to the actual sCT images. Fig. 1 illustrates the relationship between actual sCT, denoted by low-energy-resolution (LER) imaging, and SER imaging by respectively plotting the multi-energy values of corresponding pixels in the LER and SER images. For one pixel in the reconstructed LER images (*e.g.* yellow asterisks in the left of Fig. 1, designated as $\boldsymbol{y_L} \in \mathcal{R}^{B_L}$), it has 5 values for 5 energy bins, *i.e.* $B_L = 5$. While for the corresponding SER pixel (yellow points in the right of Fig. 1, designated as $\boldsymbol{y_S} \in \mathcal{R}^{B_S}$), it can have much more values, *e.g.* 50 values for $B_S = 50$ (30 - 80 keV). Note that the choice of 50 bins corresponds to the most precise μ_m we can get from NIST [18]. That is, μ is sampled every 1 keV.

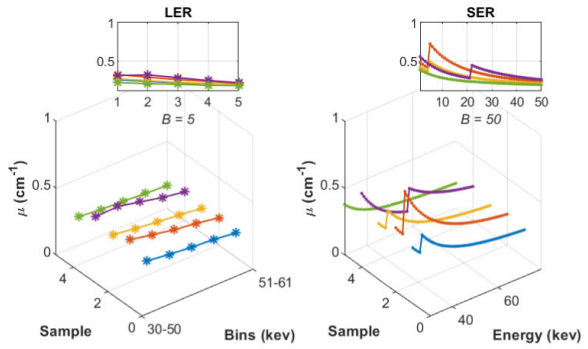

FIGURE 1. Linear attenuation coefficients: LER (left) and SER (right). Curves with different colors denote different pixels; corresponding LER and SER pixels have the same color.

The proposed SER imaging is achieved by introducing the assumption that if containing the same basis materials and concentrations, the mapping between LER and SER images is determined and can be learned. We realize it by learning the relationship between physical data and simulation data and then applying it to other physical data, as illustrated in Fig. 2. The physical data are measured and reconstructed as LER images, while the corresponding SER versions are produced by simulation with similar shapes and components but more bins. Then, LER and SER spectral features are extracted and their relationship will be learned by a mapping which can be utilized to synthesize SER images for other *in vivo* data.

C. SER IMAGE SYNTHESIS BASED ON COUPLED DICTIONARY LEARNING

We learn the mapping between LER and SER spectral features by utilizing CDL method in a pixel-wise way.

1) PIXEL-WISE TRAINING STRATEGY

It is inefficient to directly learn the mapping from the whole LER and SER images or patches. In general, learning morphological features of certain organ is another challenge that demands abundant images with various spatial information for training. It will be expensive to produce these kinds of physical data currently. Meanwhile, complex material components can make the learning more difficult.

We solve it by training the mapping from LER and SER pixel pairs, rather than the whole images or patches. With this strategy, the training samples only contain spectral information. Correspondingly, the physical phantoms used in our work can have simple shapes, but abundant material components.

Meanwhile, to cope with the difficulty of extracting features from noisy LER pixels, we enhance the learning by adding conventional CT images. The conventional CT images of physical phantoms are measured on the same sCT system but reconstructed with full spectrum (*i.e.* a single energy reconstruction), thus having lower noise level compared to that with single energy bin. The conventional CT and sCT pixels are then concatenated together as one LER sample for training. As a result, now $\boldsymbol{y_L} \in \mathcal{R}^{(B_L+1)}$ is a combined LER pixel.

2) LEARN THE MAPPING BY CDL

CDL was used in the field of super spatial resolution [19], [20]. In the theory of dictionary learning, features of a pixel $\boldsymbol{y}$ can be represented as a sparse combination of atoms inside an over-complete dictionary $\boldsymbol{D}$. That is, $\boldsymbol{y} = \boldsymbol{D\alpha}$, where $\boldsymbol{\alpha}$ is the sparse codes with very few nonzero entries:

$$argmin\|\boldsymbol{\alpha}\|_0, \quad s.t. \quad \|\boldsymbol{y} - \boldsymbol{D\alpha}\|_2^2 \leq \epsilon, \tag{5}$$

where $\|\boldsymbol{\alpha}\|_0$ designates L_0 norm of $\boldsymbol{\alpha}$. Generally, solving optimization problem in (5) is NP-hard, and it can be instead solved using L_1 norm, as:

$$\underset{\boldsymbol{\alpha}}{argmin}\|\boldsymbol{y} - \boldsymbol{D\alpha}\|_2^2 + \lambda\|\boldsymbol{\alpha}\|_1, \tag{6}$$

where λ denotes the Lagrange multiplier.

LER and SER pixel sets can then be separately represented using a LER dictionary $\boldsymbol{D_L}$ and a SER dictionary $\boldsymbol{D_S}$:

$$\begin{aligned} &\underset{\boldsymbol{\Lambda_L}}{argmin}\|\boldsymbol{Y_L} - \boldsymbol{D_L\Lambda_L}\|_F^2 + \lambda_L\|\boldsymbol{\Lambda_L}\|_1, \\ &\underset{\boldsymbol{\Lambda_S}}{argmin}\|\boldsymbol{Y_S} - \boldsymbol{D_S\Lambda_S}\|_F^2 + \lambda_S\|\boldsymbol{\Lambda_S}\|_1, \end{aligned} \tag{7}$$

where $\boldsymbol{Y_L} \in \mathcal{R}^{(B_L+1)\times N_t}$ and $\boldsymbol{Y_S} \in \mathcal{R}^{B_S\times N_t}$ respectively designate the LER and SER pixel sets with N_t pixels in the training set, $\boldsymbol{D_L} \in \mathcal{R}^{(B_L+1)\times N_D}$ and $\boldsymbol{D_S} \in \mathcal{R}^{B_S\times N_D}$ the LER and SER dictionaries containing N_D atoms, $\boldsymbol{\Lambda_L}$ and $\boldsymbol{\Lambda_S}$ the corresponding sparse codes (*i.e.* sets of α in equation (5) and (6)), and $\|\boldsymbol{Y} - \boldsymbol{D\Lambda}\|_F^2$ the data fidelity term determined by Frobenius-Norm $\|\cdot\|_F$. Then, the connection between LER and SER features is established by jointly training $\boldsymbol{D_L}$ and $\boldsymbol{D_S}$, formulated as:

$$\begin{aligned} &\underset{\widetilde{\boldsymbol{\Lambda}},\widetilde{\boldsymbol{D}}}{argmin}\|\widetilde{\boldsymbol{Y}} - \widetilde{\boldsymbol{D}}\widetilde{\boldsymbol{\Lambda}}\|_F^2 + \lambda\|\widetilde{\boldsymbol{\Lambda}}\|_1, \\ &s.t.\ \widetilde{\boldsymbol{Y}} = \begin{bmatrix} \boldsymbol{Y_S} \\ \boldsymbol{Y_L} \end{bmatrix}, \widetilde{\boldsymbol{D}} = \begin{bmatrix} \boldsymbol{D_S} \\ \boldsymbol{D_L} \end{bmatrix}, \widetilde{\boldsymbol{\Lambda}} = \begin{bmatrix} \boldsymbol{\Lambda_S} \\ \boldsymbol{\Lambda_L} \end{bmatrix}. \end{aligned} \tag{8}$$

Meanwhile, a transform matrix is utilized to decrease the impacts of dramatic gap between simulation and physical data:

$$\boldsymbol{\Lambda_S} = \boldsymbol{W\Lambda_L}, \tag{9}$$

where $\boldsymbol{W}$ denotes the transform matrix that was firstly introduced in super spatial resolution for stable cross-style image synthesis [20]. The enhanced training model then becomes:

$$\begin{aligned} &\underset{\boldsymbol{D},\boldsymbol{\Lambda},\boldsymbol{W}}{argmin}\|\boldsymbol{Y_S} - \boldsymbol{D_S\Lambda_S}\|_F^2 + \|\boldsymbol{Y_L} - \boldsymbol{D_L\Lambda_L}\|_F^2 \\ &+ \gamma\|\boldsymbol{\Lambda_S} - \boldsymbol{W\Lambda_L}\|_F^2 + \lambda_W\|\boldsymbol{W}\|_F^2 + \lambda_S\|\boldsymbol{\Lambda_S}\|_1 + \lambda_L\|\boldsymbol{\Lambda_L}\|_1. \end{aligned} \tag{10}$$

We solve the above model by alternating-direction-method-of-multipliers (ADMM), which alternately updates

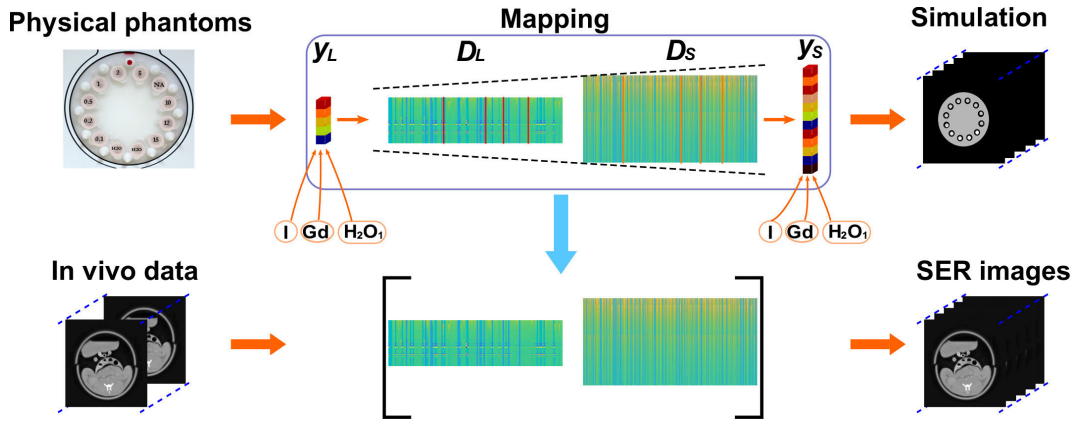

FIGURE 2. Illustration of SER based sCT imaging.

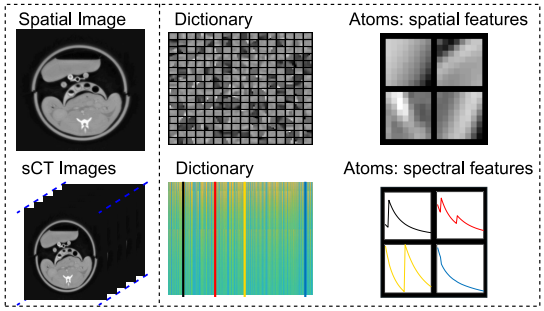

FIGURE 3. Features Learned with dictionary learning method for super spatial resolution and super energy resolution. Note that the dictionary for sCT images (lower) is the SER dictionary.

coupled dictionaries $\widetilde{\boldsymbol{D}}$, sparse codes $\widetilde{\boldsymbol{\Lambda}}$ and transform matrix $\boldsymbol{W}$.

It should be noted that atoms in the dictionaries learned using a pixel-wise strategy are energy-dependent, in contrary to spatial features in traditional super-spatial-resolution applications. Figure 3 illustrates the difference between super spatial resolution and super energy resolution by showing the learned features in practice. Atoms learned from a spatial image are morphological features, while for SER, atoms in the dictionary are energy-dependent and look more like μ curves.

After training, we can readily synthesize SER pixel $\hat{\boldsymbol{y}}_{\boldsymbol{S}}$ from its LER version $\boldsymbol{y}_{\boldsymbol{L}}$ with the learned coupled dictionaries and transform matrix, by solving the following optimization:

$$\begin{aligned}&\mathbb{SER}(\boldsymbol{y}_{\boldsymbol{L}} \rightarrow \hat{\boldsymbol{y}}_{\boldsymbol{S}}):\\ &\underset{\hat{\boldsymbol{y}}_{\boldsymbol{S}}}{argmin}\|\hat{\boldsymbol{y}}_{\boldsymbol{S}} - \boldsymbol{D}_{\boldsymbol{S}}\boldsymbol{\alpha}_{\boldsymbol{S}}\|_F^2 + \|\boldsymbol{y}_{\boldsymbol{L}} - \boldsymbol{D}_{\boldsymbol{L}}\boldsymbol{\alpha}_{\boldsymbol{L}}\|_F^2\\ &\qquad + \gamma\|\boldsymbol{\alpha}_{\boldsymbol{S}} - \boldsymbol{W}\boldsymbol{\alpha}_{\boldsymbol{L}}\|_F^2 + \lambda_S\|\boldsymbol{\alpha}_{\boldsymbol{S}}\|_1 + \lambda_L\|\boldsymbol{\alpha}_{\boldsymbol{L}}\|_1. \quad (11)\end{aligned}$$

The above model is also solved by ADMM.

D. MATERIAL DECOMPOSITION USING SER IMAGES

The synthesized SER images are then utilized for material decomposition in image domain.

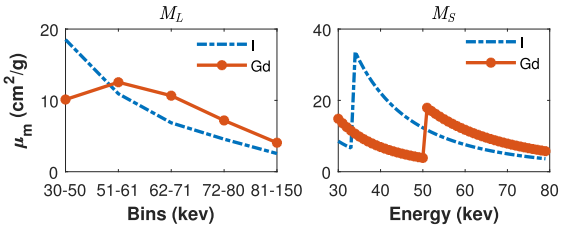

FIGURE 4. Mass attenuation coefficients in M_L and M_S for iodine and gadolinium.

For existing sCT, decomposition matrix $\boldsymbol{M}$ is generally initialized by the aforementioned $\dot{\mu}_m$ [7] according to:

$$\dot{\mu}_{m\alpha}(i) = \frac{\int_{E\in E_i} n_0(E)d_i(E)\mu_{m\alpha}(E)dE}{\int_{E\in E_i} n_0(E)d_i(E)dE}, \quad i = 1, \ldots, B, \tag{12}$$

where $\mu_{m\alpha}(E)$ designates the theoretical MAC value and E_i the width of the i-th bin. Note that $\dot{\mu}_m(i)$ is an estimate of the true value of $\mu_m(i)$ corresponding to the i-th bin. As a result, thinner bins can produce more precise $\dot{\mu}_{m\alpha}(i)$, *i.e.* more precise $\boldsymbol{M}$. A more precise decomposition matrix suitable for the SER images is then needed. For LER, $\boldsymbol{\mu_m}$ of each basis material (one column of $\boldsymbol{M}$ in equation (4) designated as $\boldsymbol{M_L}$) is an effective value at B_L energy bins. In contrast, $\boldsymbol{M}$ for SER (designated as $\boldsymbol{M_S}$) has much more energy bins, *e.g.* $B_S = 50$. Both $\boldsymbol{M_L}$ and $\boldsymbol{M_S}$ have the same material components, *e.g.* iodine (I), gadolinium (Gd) and water in our experiment. Each column of $\boldsymbol{M_S}$ is a more precise value directly retrieved from NIST, as illustrated in Fig. 4.

To assess the decomposition of the synthesized SER images, we choose a common image-domain decomposition algorithm using L_1 norm (lasso) regularization for both SER and LER images, which can reduce time complexity, preventing the model from over-fitting. Note that to illustrate the advantage of SER imaging, we focus on the comparison between SER and LER images, rather than different decomposition methods, *i.e.* only L1 method is considered in this work. Mathematically, we formulate the SER-based material

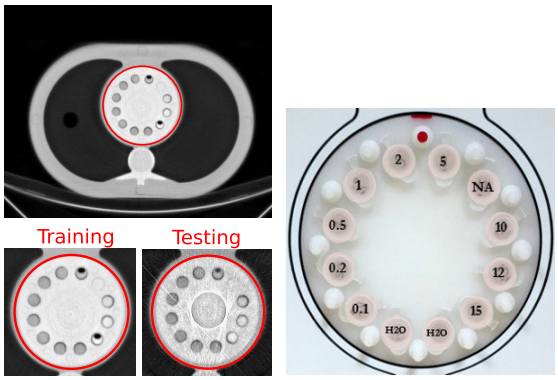

(a) (b)

FIGURE 5. (a) Reconstructed image (at 1st bin) of physical phantom for training (upper) and ROIs (areas inside red contour) for training and testing (lower). Note that the phantoms for training and testing have different noise levels due to the presence of extensional fat rings added to the testing phantom exterior. (b) inserts: labels designate the concentration in each disk (unit: mg/cc).

decomposition using lasso as:

$$\hat{\boldsymbol{x}} = \underset{\boldsymbol{x}}{argmin} \|\hat{\boldsymbol{y}}_{\boldsymbol{S}} - \boldsymbol{M}_{\boldsymbol{S}}\boldsymbol{x}\|_F^2 + \lambda\|\boldsymbol{x}\|_1. \tag{13}$$

III. EXPERIMENTS AND RESULTS

A. EXPERIMENTAL SETTING AND EVALUATION METRICS

The experiments were carried on real data from a Philips sCT prototype [21]–[23]. This medical approved prototype has a 500mm FOV and a pixel pitch of 0.274mm at iso-center. The photon-counting detector has a 1848 × 64 grid. However we used a 2 × 8 binning mode to obtain 924×8 pixels with a size of 1 × 2mm. The experiments were performed at tube voltage 120 kVp and current 220 mA under rotation time of 1s with a small focal spot. The volumetric CT dose index (CDTIvol) was 22.2 mGy. The system acquires 2400 projections per rotation. It has 5 energy thresholds set to 30, 51, 62, 72, 81 keV. These values have been selected to optimize the Gadolinium k-edge imaging and are the same for all the physical data in the present work. This configuration leads to 5 energy bins: #1[30-51keV], #2[51-62keV], #3[62-72keV], #4[72-81keV] and #5[81-120keV].

Reconstructed images from one single bin are shown in Fig. 5a. Fig. 5b depicts the cylindrical inserts of the physical phantom. The upper image in Fig. 5a is for training, while the lower two regions-of-interests (ROIs) of phantoms (*i.e.* all the areas inside red contours) are for training and testing, respectively. Training and testing sets do not share the same pixels. The reconstructed images for training and testing have different noise levels due to the presence of extensional fat rings added to the testing phantom exterior. Removable tubes containing different dilutions of iodine or gadolinium are inserted in the ROIs, as illustrated in Fig. 5b. The number refers to the concentration of each tube which covers from 0.1 mg/cc to 15 mg/cc. In our experiments, both iodine and gadolinium were measured for training and testing. Meanwhile, we use another *in vivo* dataset to further evaluate the proposed method. In our experiments, a rabbit

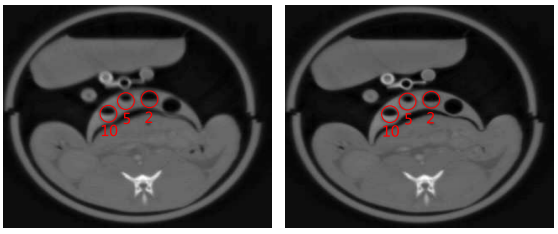

(a) (b)

FIGURE 6. The reconstructed image of rabbit after injection of Gd dilution (at 1st bin): (a) 5 minutes and (b) 15 minutes. Labels in ROIs designate the nominal concentration (mg/cc).

was injected by gadolinium dilution, the image of which 5 and 15 minutes after the injection are respectively given in Fig. 6. For quantitative evaluation, tubes with known concentrations of gadolinium (2, 5, 10 mg/cc) are also placed beside the rabbit. The image of 5 min after injection is a little blurred due to movement.

All the spatial images in physical datasets were separately reconstructed at each energy bin via a common reconstruction method: conjugate gradient method (with Reconstruction Toolkit (RTK) [24]). Note that the decomposition method of Philips prototype is projection-domain based, while our proposed SER-based method is performed in image domain. What's more, our reconstruction software (RTK) is also different from that used by Philips. In other words, we apply our own algorithms on prepped photon count data from the scanner, whereas other correction steps from the Philips image chain (*e.g.* proper handling of bad detectors) are not used. Hence the results will be different from the Philips' reconstruction results. The detector bin response function $d_i(E)$ in model (2) was provided by Philips. All phantoms were reconstructed into 9 slices and the size of each slice is 900*900. We learned the coupled dictionaries composed of 1024 (N_D) atoms from 400K (N_t) random LER-SER pixel pairs. On a machine equipped with Nvidia Tesla V100 and Intel I9 CPU, our method took 18h for training and 5 minutes for testing of one slice.

Both SER images synthesis and material decomposition were quantitatively evaluated. Normalized Root Mean Square Error (NRMSE) (*i.e.* $NRMSE = RMSE/\bar{x}$ for the image x) and peak signal-to-noise ratio (PSNR) were utilized to assess the quality of synthesized SER images. Note that NRMSE and PSNR were respectively calculated on the whole images of iodine and gadolinium, in order to assess the total synthesis performance of all concentrations. The smaller the NRMSE and the higher the PSNR, the more accurate the synthesis.

Mean and standard error of the mean (SEM) were calculated for each dilution to assess decomposition accuracy. Meanwhile, linear regression between the nominal (y-axial) and measured concentrations (using the calculated mean values, x-axial) was performed for all dilutions, as: $y = ax + b$, where a and b represent the slope and y-intercept, respectively. To further assess the detection ability of contrast agents, we also calculated the limit of detection (LOD) for

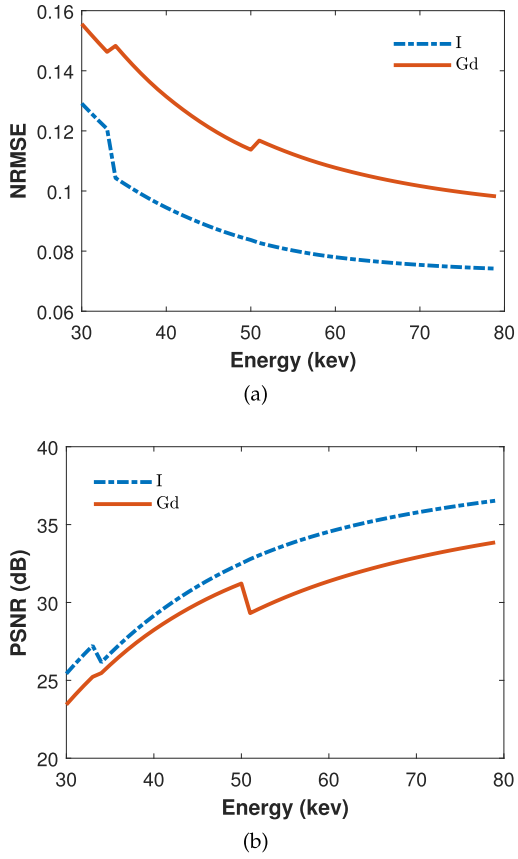

FIGURE 7. The (a) NRMSE and (b) PSNR of synthesized SER images for I and Gd in training.

both iodine and gadolinium. The LOD was described by the Clinical and Laboratory Standards Institute [25] as:

$$LOB = \bar{x}_{blank} + 1.645\delta_{blank},$$
$$LOD = \frac{LOB - b}{a}, \tag{14}$$

where $\bar{x}_{blank}$ denotes mean water signal detected in the images of decomposed contrast agents, δ_{blank} the standard deviation of the measurement, and LOB the limit of blank. LOB denotes the highest apparent contrast agent concentration expected to be found when replicates of a sample contain no contrast agent, which was calculated using tubes of water in each phantom. LOD is taken as the lowest concentration of a contrast agent in a sample that can be detected.

B. TRAINING

NRMSE and PSNR (dB) of synthesized SER images at each energy bin are illustrated in Fig. 7. SER images of iodine have relatively higher accuracy than gadolinium, *e.g.* smaller NRMSE and higher PSNR, although both of them have good synthesis performance. Note that low-energy bins have relatively larger NRMSE and smaller PSNR, especially for bins of k-edge (*i.e.* energy bins containing k-edge). Also, we need to recover more details in the first two bins: 30 - 50 keV and 51 - 61 keV.

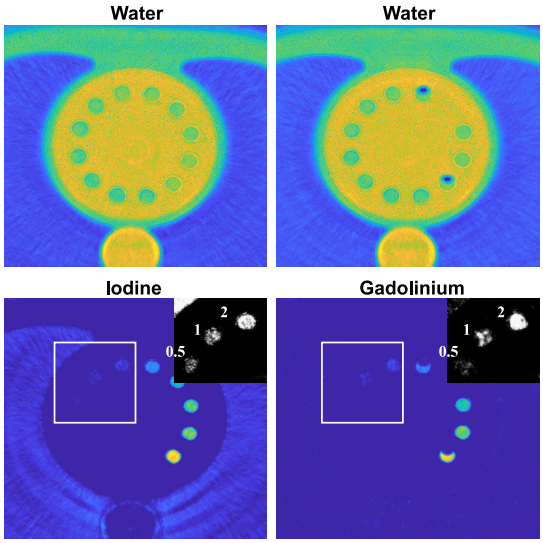

FIGURE 8. The decomposition results of SER based method on physical phantoms in training. Note that ROIs are shown in grayscale to highlight morphological information. Labels in ROIs denote the dilution concentration (mg/cc).

The material decomposition results based on synthesized SER images are shown in Fig. 8. Visually, the proposed SER-based decomposition presents good detection ability according to the edge-preserving performance in training. It can substantially preserve edge information even for low-concentration iodine and gadolinium *e.g.* 0.5 mg/cc, as illustrated in the ROIs. Note that all the ROIs are shown with grayscale images in order to highlight morphological information.

To quantitatively assess the decomposition, linear regressions of iodine and gadolinium for all the concentrations are illustrated in Fig. 9. Note that there is no additional scatter correction for all the results of linear regression in this work. Both iodine and gadolinium have clearly high accuracy with respect to theoretical concentrations. The correlations between the measured and prepared concentrations are strongly linear for all dilutions (all $R^2 \geq 0.95$). The slopes are close to 1 for both iodine ($a = 0.96$) and gadolinium ($a = 0.97$). The y-intercept values are very low, *e.g.* $b = -0.26$ for iodine and -0.38 for gadolinium. Additionally, the decomposition is very reliable because both iodine and gadolinium are always underestimated and their SEMs are small.

Table 1 lists LOD for both iodine and gadolinium, to further assess the detection limit. Both iodine and gadolinium can be detected for concentrations lower than 0.5 mg/cc in training. More specifically, the proposed SER method has better detection ability for iodine than for gadolinium.

C. TESTING

The LER-based material decomposition method using the same lasso regularization was compared to the proposed SER-based method. Both physical phantoms with more noise and artifacts and *in vivo* data were tested.

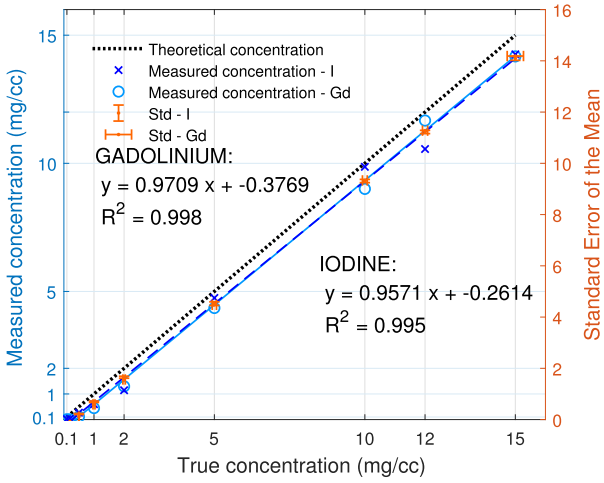

FIGURE 9. The linear-regression results of iodine and gadolinium for SER-based material decomposition in training: linear regression model, R-squared (R^2) and standard error of the mean (SEM).

TABLE 1. The LOD of different material decomposition methods on physical phantoms.

	LER	SER	
		Training	Testing
I	2.00	0.34	0.56
Gd	4.81	0.45	0.84

SER images were generated through equation (11). Fig. 10 shows the NRMSE and PSNR (dB) of synthesized SER images at each energy bin for testing. As in the case of training, SER images of iodine have relatively higher accuracy than gadolinium, *e.g.* smaller NRMSE and higher PSNR. Compared to training, although testing has relatively higher NRMSE and smaller RSNR, the difference is small.

The material decomposition results of physical phantoms with more noise and artifacts are shown in Fig. 11. In contrast to LER method, the proposed SER method shows better performance in quantification and detection compared to LER method. Firstly, the proposed SER method gives much better morphological accuracy in terms of edge-preserving performance and much less noise, even for low-concentration materials, *e.g.* 0.5 mg/cc for both iodine and gadolinium. The edges are substantially preserved by SER method. While for LER method, the selected areas of low-concentration materials are overwhelmed by noise and cannot be detected.

Secondly, more quantitatively as shown in Fig. 12, linear regressions of both I and Gd illustrate that SER-based method has much smaller errors. SER method presents more precise slope (for iodine: $a_{LER} = 0.71$ and $a_{SER} = 0.87$; for gadolinium: $a_{LER} = 1.24$ and $a_{SER} = 0.94$) and y-intercept value (for iodine: $b_{LER} = 1.71$ and $b_{SER} = -0.08$; for gadolinium: $b_{LER} = 0.92$ and $b_{SER} = -0.51$). Meanwhile, SER method is more reliable with smaller SEMs and almost all decomposed values always exhibit the same underestimation trend. As can be observed in Table 1 that lists LOD values of different methods for both iodine and gadolinium, our SER method has

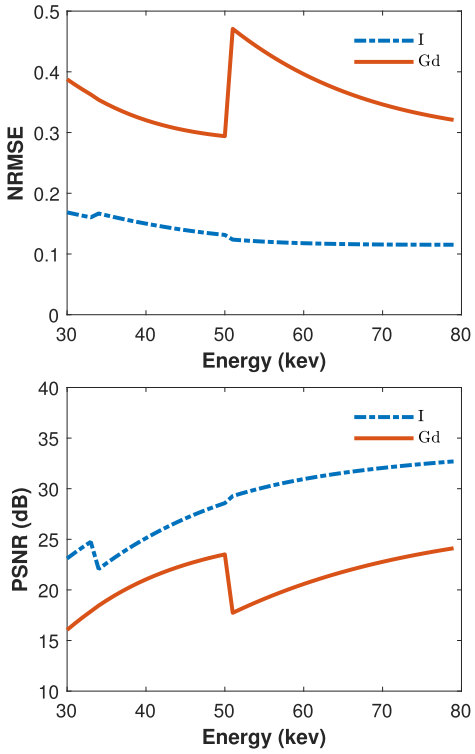

FIGURE 10. The NRMSE and PSNR of synthesized SER images for I and Gd in testing.

TABLE 2. The mean and standard error of the mean (SEM) of each tube in *in vivo* data (15 min after injection of gadolinium).

	LER	SER
True Conc. (mg/cc)	mean+SEM	
10	9.2 + 0.05	10.0+ 0.05
5	3.3 + 0.01	4.4 + 0.01
2	0.6 + 0.01	1.9 + 0.01

much stronger detection ability for both iodine and gadolinium compared to LER method by producing smaller LOD values in testing. It has better detection ability for iodine than for gadolinium, as in the case of training.

Meanwhile, the decomposition results of different methods on *in vivo* data are given in Fig. 13. We identify calcium (Ca) inside spine as the basis material iodine in terms of their similar MAC under our energy-thresholds arrangement. Clearly, LER method has less accurate separation between gadolinium and iodine and has more noise for the two basis materials. In contrast, the SER method has better detection ability for both iodine (in the spine) and gadolinium (in tubes and organs). Mean and SEM of gadolinium in the tubes are listed in Table 2. Obviously, SER method leads to more accurate decomposition for gadolinium of concentrations covering from 10 mg/cc to 2 mg/cc.

IV. DISCUSSION

Our main goal is to improve the energy resolution of sCT in order to improve the k-edge quantification accuracy and detection ability. To achieve that we introduced the notion

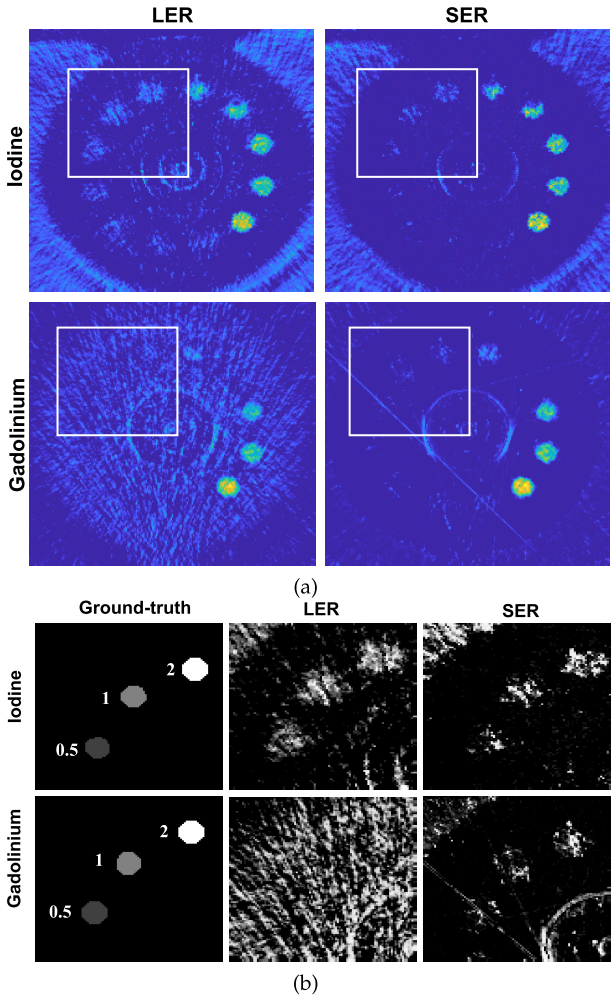

FIGURE 11. (a) The decomposition results of different methods on physical phantoms in testing; (b) the ROIs in (a) for low-concentration materials.

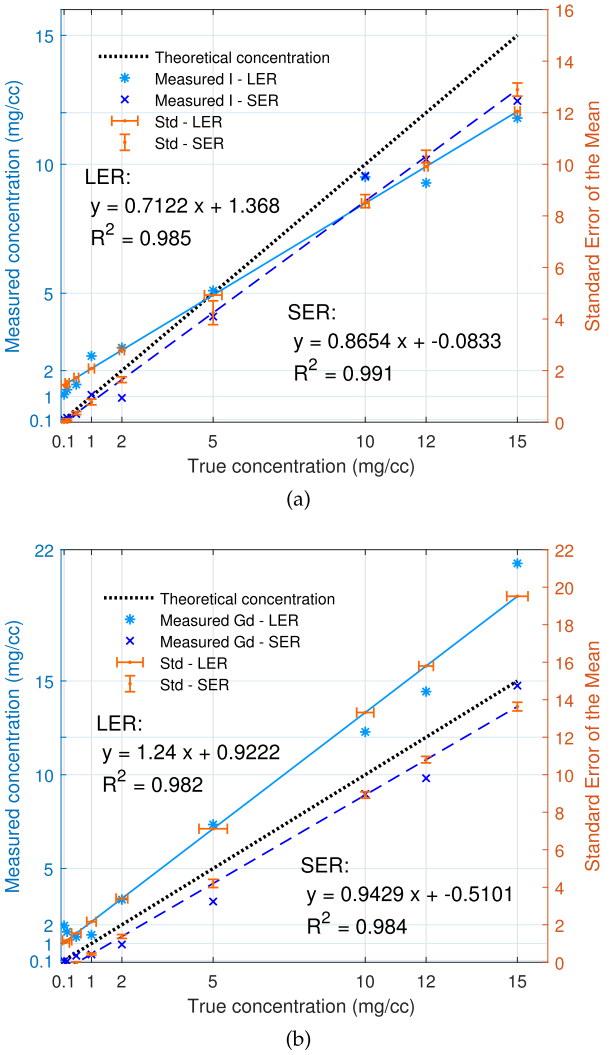

FIGURE 12. The linear regression results of (a) iodine and (b) gadolinium for different material decomposition methods in testing: linear regression model, R-squared (R^2) and standard error of the mean (SEM).

of SER in sCT to achieve SER imaging, by fully exploiting abundant spectral features embedded in both simulation and physical data. Preliminary results revealed that the proposed SER method enables accurate decomposition and high detection ability even for low-concentration materials.

The SER-based material decomposition method is reliable. Firstly, even for noisier conditions in training, the proposed SER method still enables high decomposition accuracy and detection ability. In our experiments, we trained the dictionaries on the phantoms with less noise and artifacts, but tested on the ones with stronger noise and more artifacts. However, the results still show better decomposition accuracy and detection ability of the proposed method compared to the LER method, especially for iodine. Secondly, accurate decomposition of *in vivo* data polluted by movement (5 min after the injection) also shows the reliability of our method. Moreover, the decomposition results of both iodine and gadolinium depict consistency, albeit being underestimated for almost all concentrations.

In this work, we did not consider the mixtures of multiple elements in the experiments. Nevertheless, materials detection mainly relies on the subsequent decomposition method if the input is SER images. In this sense, accurate SER images are primordial for high material decomposition accuracy. At the same time, the ability of the decomposition method with L1 norm to detect mixtures has been demonstrated in [26], [27]. Hence, our method would work for the mixtures of interested elements (I or Gd). For other possible mixtures or multiple different contrast agents, *e.g.* bone/calcium basis, soft-tissue/water basis, corresponding training is necessary for ensuring the decomposition performance, which deserves further research in the future work.

Concerning the partial volume effect, which arises when more than one material type occurs in a voxel (or pixel) having a limited spatial resolution, it is a very interesting and pertinent issue in sCT. In our method, material decomposition is processed pixel by pixel, which implies that only material category and density are accounted for and spatial neighborhood is not involved. As a result, partial volume effect

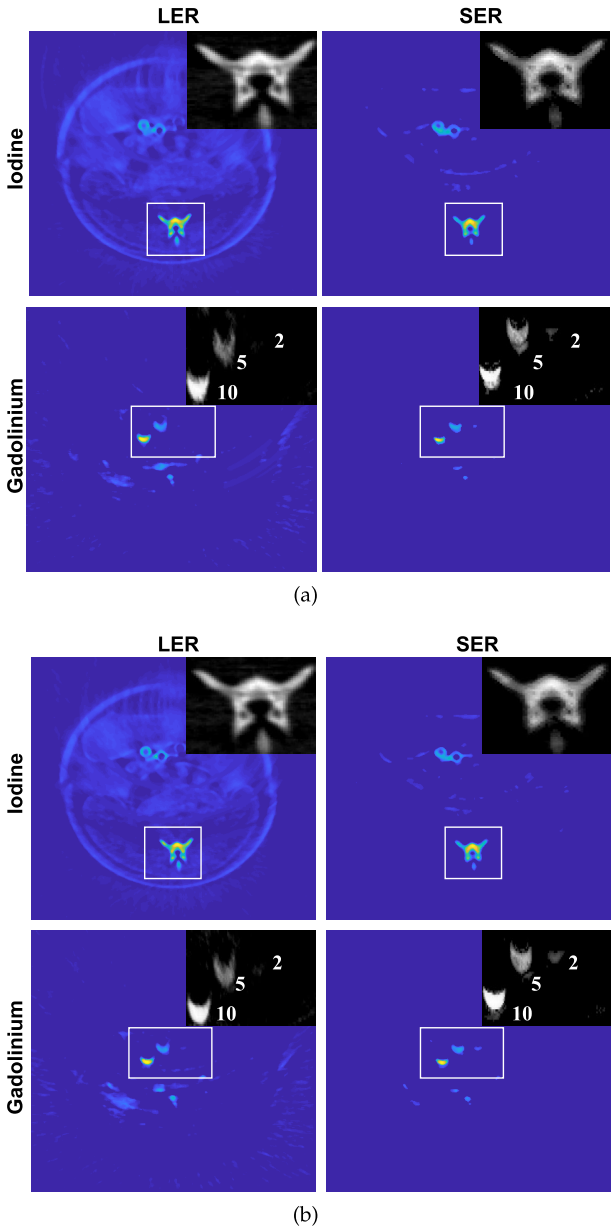

FIGURE 13. The decomposition results of different methods on in vivo data in testing: (a) 5 min after the injection of contrast agents; (b) 15 min after. Note that calcium in spine is treated as iodine, and the basis material gadolinium exists in tubes and organs. The Numbers ('2', '5' and '10') refer to the concentrations in unit mg/cc.

would be minimized. Nevertheless, it would be interesting to study how a decomposed material quantitatively changes with different spatial resolutions, different types of mixtures, different material proportions in the voxel, *etc*.

The interest of projection-domain and one-step methods lies in the fact that they generate directly material images from projection data without needing to first reconstruct spatial images. In contrast, image-domain decomposition has its own advantages of being able to both exploit spatial images and generate material images. On the other hand, projection data is not always available or not practical to use in clinical practice because of commercial confidentiality or practical constraints. In short, image-domain methods are hardware-independent and thus provide much flexibility than the other 2 methods.

Note that the accuracy of material decomposition is also conditioned by the limitations of PCDs, such as K-escape, pulse pileup, and charge sharing effects. Some PCDs can remove all the photons, which are under the lowest threshold before any charge sharing corrections causing incorrectly binned photons. Similarly, a shift in the energy of the measured photons (when over 40 keV) is possible, *e.g.*, 60 keV photon is measured around 70 keV and is then binned in the wrong energy bin. To take into account the above-mentioned issues, a more sophisticated simulation of common problems seen in PCDs might be interesting, which would allow us to get insights into how the limitations of PCDs affect the accuracy of the SER-based material decomposition method.

Each single synthesized SER image is a virtual monochromatic image (mono-E). The mono-E image form DECT is generally reconstructed from a pair of decomposed basis material images (*e.g.* a soft-tissue-like basis material and a contrast agent). The performance of mono-E is determined by the material decomposition that is processed only on actual images (LER images for sCT in the present study). In contrast, SER images are directly synthesized using spectral features learned from both simulation and physical data. As a result, our method could contribute to more accurate mono-E imaging.

V. CONCLUSION

We have proposed a SER imaging method to improve image-domain material decomposition in sCT. The method is based on generating SER images from LER images. This is achieved through learning mapping between simulation and physical data in a pixel-wise way and applying it to other physical data. The results on both physical phantoms and in vivo data showed that the SER-based material decomposition method resulted in a clearly more accurate material decomposition and a higher detection ability as compared to the LER-based method. In the future work, the performance of other image-domain decomposition methods using SER images will be investigated. It would be also interesting to compare image-domain decomposition with projection-domain methods such as that used by Philips sCT prototype.

ACKNOWLEDGMENT

The authors thank Dr. Klaus Erhard and Dr. Yoad Yagil for the careful reading of the manuscript and many helpful comments.

REFERENCES

[1] M. C. Jacobsen, E. N. K. Cressman, E. P. Tamm, D. L. Baluya, X. Duan, D. D. Cody, D. Schellingerhout, and R. R. Layman, "Dual-energy CT: Lower limits of iodine detection and quantification," *Radiology*, vol. 292, no. 2, pp. 414–419, Aug. 2019.

[2] B. Xie, "Image-domain material decomposition in spectral photon-counting CT for medical applications," Ph.D. dissertation, Dept. EEA, Univ. Lyon, France, 2020.

[3] J. P. Schlomka, E. Roessl, R. Dorscheid, S. Dill, G. Martens, T. Istel, C. Bäumer, C. Herrmann, R. Steadman, and G. Zeitler, "Experimental feasibility of multi-energy photon-counting K-edge imaging in pre-clinical computed tomography," *Phys. Med. Biol.*, vol. 53, no. 15, pp. 4031–4047, 2008.
[4] N. Ducros, J. F. P.-J. Abascal, B. Sixou, S. Rit, and F. Peyrin, "Regularization of nonlinear decomposition of spectral X-ray projection images," *Med. Phys.*, vol. 44, no. 9, pp. e174–e187, Sep. 2017.
[5] T. Su, V. Kaftandjian, P. Duvauchelle, and Y. Zhu, "A spectral X-ray CT simulation study for quantitative determination of iron," *Nucl. Instrum. Methods Phys. Res. A, Accel. Spectrom. Detect. Assoc. Equip.*, vol. 894, pp. 39–46, Jun. 2018.
[6] Y. Zhang, X. Mou, G. Wang, and H. Yu, "Tensor-based dictionary learning for spectral CT reconstruction," *IEEE Trans. Med. Imag.*, vol. 36, no. 1, pp. 142–154, Jan. 2017.
[7] H. Q. Le and S. Molloi, "Least squares parameter estimation methods for material decomposition with energy discriminating detectors," *Med. Phys.*, vol. 38, no. 1, pp. 245–255, Jan. 2011.
[8] C. J. Bateman, D. Knight, B. Brandwacht, J. M. Mahon, J. Healy, R. Panta, R. Aamir, K. Rajendran, M. Moghiseh, M. Ramyar, and D. Rundle, "MARS-MD: Rejection based image domain material decomposition," *J. Instrum.*, vol. 13, no. 5, May 2018, Art. no. P05020.
[9] W. Xia, W. Wu, S. Niu, F. Liu, J. Zhou, H. Yu, G. Wang, and Y. Zhang, "Spectral CT reconstruction—ASSIST: Aided by self-similarity in image-spectral tensors," *IEEE Trans. Comput. Imag.*, vol. 5, no. 3, pp. 420–436, Sep. 2019.
[10] Z. Chen and L. Li, "Robust multimaterial decomposition of spectral CT using convolutional neural networks," *Opt. Eng.*, vol. 58, no. 1, p. 1, Jan. 2019.
[11] W. Wu, P. Chen, V. V. Vardhanabhuti, W. Wu, and H. Yu, "Improved material decomposition with a two-step regularization for spectral CT," *IEEE Access*, vol. 7, pp. 158770–158781, 2019.
[12] R. F. Barber, E. Y. Sidky, T. G. Schmidt, and X. Pan, "An algorithm for constrained one-step inversion of spectral CT data," *Phys. Med. Biol.*, vol. 61, no. 10, pp. 3784–3818, 2016.
[13] K. Mechlem, S. Ehn, T. Sellerer, E. Braig, D. Münzel, F. Pfeiffer, and P. B. Noël, "Joint statistical iterative material image reconstruction for spectral computed tomography using a semi-empirical forward model," *IEEE Trans. Med. Imag.*, vol. 37, no. 1, pp. 68–80, Jan. 2018.
[14] C. Mory, B. Sixou, S. Si-Mohamed, L. Boussel, and S. Rit, "Comparison of five one-step reconstruction algorithms for spectral CT," *Phys. Med. Biol.*, vol. 63, no. 23, Nov. 2018, Art. no. 235001.
[15] Y. Iyama, T. Nakaura, A. Iyama, K. Katahira, and Y. Yamashita, "The usefulness of dual-layer spectral computed tomography for myelography: A case report and review of the literature," *Case Rep. Orthopedics*, vol. 2018, pp. 1–4, Mar. 2018.
[16] S. Leng, L. Yu, J. Wang, J. G. Fletcher, C. A. Mistretta, and C. H. McCollough, "Noise reduction in spectral CT: Reducing dose and breaking the trade-off between image noise and energy bin selection," *Med. Phys.*, vol. 38, no. 9, pp. 4946–4957, 2011.
[17] S. Si-Mohamed, D. Bar-Ness, M. Sigovan, V. Tatard-Leitman, D. P. Cormode, P. C. Naha, P. Coulon, L. Rascle, E. Roessl, M. Rokni, A. Altman, Y. Yagil, L. Boussel, and P. Douek, "Multicolour imaging with spectral photon-counting CT: A phantom study," *Eur. Radiol. Exp.*, vol. 2, no. 1, p. 34, Dec. 2018.
[18] E. Saloman and J. Hubbell, "X-ray attenuation coefficients (total cross sections): Comparison of the experimental data base with the recommended values of Henke and the theoretical values of scofield for energies between 0. 1-100 keV," Nat. Bur. Standards, Washington, DC, USA, Tech. Rep. NBSIR–86-3431, Jul. 1986.
[19] J. Yang, J. Wright, T. S. Huang, and Y. Ma, "Image super-resolution via sparse representation," *IEEE Trans. Image Process.*, vol. 19, no. 11, pp. 2861–2873, Nov. 2010.
[20] S. Wang, L. Zhang, Y. Liang, and Q. Pan, "Semi-coupled dictionary learning with applications to image super-resolution and photo-sketch synthesis," in *Proc. IEEE Conf. Comput. Vis. Pattern Recognit. (CVPR)*, Jun. 2012, pp. 2216–2223.
[21] N. R. van der Werf, S. Si-Mohamed, P. A. Rodesch, R. W. van Hamersvelt, M. J. W. Greuter, S. Boccalini, J. Greffier, T. Leiner, L. Boussel, M. J. Willemink, and P. Douek, "Coronary calcium scoring potential of large field-of-view spectral photon-counting CT: A phantom study," *Eur. Radiol.*, vol. 32, pp. 1–11, Jul. 2021.
[22] S. Si-Mohamed, S. Boccalini, P.-A. Rodesch, R. Dessouky, E. Lahoud, T. Broussaud, M. Sigovan, D. Gamondes, P. Coulon, Y. Yagil, L. Boussel, and P. Douek, "Feasibility of lung imaging with a large field-of-view spectral photon-counting CT system," *Diagnostic Intervent. Imag.*, vol. 102, no. 5, pp. 305–312, May 2021.
[23] S. A. Si-Mohamed, J. Greffier, J. Miailhes, S. Boccalini, P.-A. Rodesch, A. Vuillod, N. van der Werf, D. Dabli, D. Racine, D. Rotzinger, F. Becce, Y. Yagil, P. Coulon, A. Vlassenbroek, L. Boussel, J.-P. Beregi, and P. Douek, "Comparison of image quality between spectral photon-counting CT and dual-layer CT for the evaluation of lung nodules: A phantom study," *Eur. Radiol.*, vol. 32, pp. 1–9, Jun. 2021.
[24] S. Rit, M. V. Oliva, S. Brousmiche, R. Labarbe, D. Sarrut, and G. C. Sharp, "The reconstruction toolkit (RTK), an open-source cone-beam CT reconstruction toolkit based on the insight toolkit (ITK)," *J. Phys., Conf. Ser.*, vol. 489, Mar. 2014, Art. no. 012079.
[25] M. Moretti, D. Sisti, M. B. Rocchi, and E. Delprete, "CLSI EP17-A protocol: A useful tool for better understanding the low end performance of total prostate-specific antigen assays," *Clin. Chim. Acta*, vol. 412, nos. 11–12, pp. 1143–1145, May 2011.
[26] B. Xie, P. Niu, T. Su, V. Kaftandjian, L. Boussel, P. Douek, F. Yang, P. Duvauchelle, and Y. Zhu, "ROI-wise material decomposition in spectral photon-counting CT," *IEEE Trans. Nucl. Sci.*, vol. 67, no. 6, pp. 1066–1075, Jun. 2020.
[27] B. Xie, T. Su, V. Kaftandjian, P. Niu, F. Yang, M. Robini, Y. Zhu, and P. Duvauchelle, "Material decomposition in X-ray spectral CT using multiple constraints in image domain," *J. Nondestruct. Eval.*, vol. 38, no. 1, Mar. 2019, Art. no. 162019.

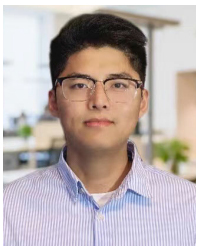

BINGQING XIE received the B.S. degree in physics from Shandong University, in 2013, the M.S. degree in microelectronics from the University of Chinese Academy of Sciences, and the Ph.D. degree from CREATIS, INSA Lyon, in 2020, under the supervision of Prof. Yuemin Zhu. His research interests include medical image processing, especially spectral CT image processing and machine learning.

YUEMIN ZHU received the B.Sc. degree in telecommunication from the Huazhong University of Science and Technology (HUST), China, in 1982, and the M.Sc. and Ph.D. degrees from INSA, Lyon, France, in 1984 and 1988, respectively, and the Habilitation à Diriger des Recherches from France, in 1993. He is currently the Permanent Research Director of the Centre National de la Recherche Scientifique (CNRS), France. His current research projects focus on human cardiac diffusion tensor imaging and human cardiac polarize light imaging. He has so far published more than 260 research papers, including 105 journal articles, two book chapters, 12 invited conference keynotes, and 147 conference proceedings. His current research interests include image representation, reconstruction, correction, denoising, registration, segmentation, visualization, and fusion. Due to his research contribution, he has received twice the French Prize of Scientifique Excellence (Prime d'Excellence Scientifique), in 2010 and 2014, respectively. He is an Editor of *Journal of Medical Engineering*, and an invited reviewer of more than 20 international journals.

PEI NIU received the Ph.D. degree from CREATIS, INSA Lyon, in 2020. Her research interests include medical image processing, deep learning, and pattern recognition.

TING SU received the Ph.D. degree from LVA, INSA Lyon, in 2018. She is currently an Associate Researcher with the Research Center for Medical Artificial Intelligence, Shenzhen Institutes of Advanced Technology, Chinese Academy of Sciences, Shenzhen, China. Her research interests include medical image processing, signal processing, and artificial intelligence.

FENG YANG received the B.S. and M.S. degrees from Northwestern Polytechnical University, China, in 2005 and 2007, respectively, and the Ph.D. degree from the National Institute of Applied Science (INSA Lyon), France, in 2011. She was working as the Principal Investigator and an Associate Professor with Beijing Jiaotong University, China, from 2012 to 2019. She joined the Lister Hill National Center for Biomedical Communications (LHNCBC), National Library of Medicine (NLM), in October 2017. She is currently a Research Fellow with NLM, NIH. She has so far published more than 70 research papers, including 30 journal articles, one book chapters, and 40 conference proceedings. Her current research interests include machine learning and artificial intelligence-based biomedical image processing and analysis, and cardiac image processing.

LIHUI WANG was born in Jilin, China, in 1982. She received the B.S. degree in electronic science and technology and the M.S. degree in optics from Harbin Engineering University, Harbin, in 2006 and 2008, respectively, and the Ph.D. degree in image and system from INSA Lyon, Lyon, France, Guizhou University, Guiyang, in 2013. From 2013 to 2017, she was an Assistant Professor with the Department of Computer Science and Technology, Guizhou University. Since 2017, she has been an Associate Professor with the Key Laboratory of Intelligent Medical Image Analysis and Precise Diagnosis, Guiyang, Guizhou. She has authored more than 30 articles. Her research interests include medical imaging, image processing, pattern recognition, and machine learning.

PIERRE-ANTOINE RODESCH received the Ph.D. degree from Leti, CEA Grenoble, in 2018. He has five years experience of spectral CT mainly for medical diagnosis. He has successively worked with the all professions involved in this device development, electronics, mathematicians, researchers, IT engineers, radiologists, and medical physicists. He currently holds a postdoctoral position at Lyon University Hospital HCL.

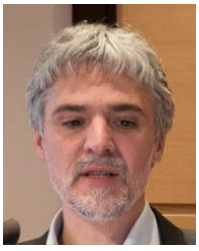

LOIC BOUSSEL is currently a Professor with CREATIS, INSA Lyon. He also works with the Department of Radiology, Hospices Civilsde1 de Lyon, France. His work focuses on medical imaging processing and its applications, especially on spectral CT.

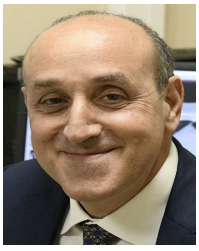

PHILIPPE DOUEK is currently a Professor with CREATIS, INSA Lyon. He also works with the Department of Radiology, Hospices Civilsde1 de Lyon, France. He is the Chairperson of a consortium of ten Departments of Radiology and Nuclear Medicine in Lyon Hospital (HCL), France. He has more than 15 years of imaging research, with many multidisciplinary projects in this field, as well as international collaboration (NIH, UCSF). He has strong experience in coordination of preclinical and clinical projects in imaging research involving clinicians, basic science researchers, imaging companies, and pharmaceutical companies.

PHILIPPE DUVAUCHELLE is currently an Associate Professor at LVA, INSA Lyon. His general skills concerns physics and a NDT methods. He is particularly an expert in techniques using X-ray, from simulation and modeling of X-rays-matter interactions up to images and signals analysis, through various types of conventional and non-conventional X-ray imaging.